



1

2

3

4

5 **Medium-range predictability of early summer sea ice thickness distribution in**  
6 **the East Siberian Sea: Importance of dynamical and thermodynamic melting**  
7 **processes**

8

9 **Takuya Nakanowatari<sup>1,\*</sup>, Jun Inoue<sup>1</sup>, Kazutoshi Sato<sup>1</sup>, Laurent Bertino<sup>2</sup>, Jiping Xie<sup>2</sup>, Mio**  
10 **Matsueda<sup>3</sup>, Akio Yamagami<sup>3</sup>, Takeshi Sugimura<sup>1</sup>, Hironori Yabuki<sup>1</sup>, and Natsuhiko Otsuka<sup>4</sup>**

11 <sup>1</sup>National Institute of Polar Research, 10-3, Midori-cho, Tachikawa-shi, Tokyo, 190-8518, Japan;

12 <sup>2</sup>Nansen Environmental and Remote Sensing Center, Thormøhlens gate 47, N-5006 Bergen,

13 Norway; <sup>3</sup>Center for Computational Sciences, University of Tsukuba, 1-1-1 Tennodai, Tsukuba,

14 Ibaraki 305-8577, Japan; <sup>4</sup>Arctic Research Center, Hokkaido University, Kita-21 Nishi-11 Kita-ku,

15 Sapporo, 001-0021, Japan

16

17 \*Corresponding author: Takuya Nakanowatari, E-mail: [nakanowatari.takuya@nipr.ac.jp](mailto:nakanowatari.takuya@nipr.ac.jp)

18



19

### Abstract

20 Accelerated retreat of Arctic Ocean summertime sea ice has focused attention on the potential use  
21 of the Northern Sea Route (NSR), for which sea ice thickness (SIT) information is crucial for safe  
22 maritime navigation. This study evaluated the medium-range (lead time below 10 days) forecast  
23 skill of SIT distribution in the East Siberian Sea (ESS) in early summer (June–July) based on the  
24 TOPAZ4 ice ocean data assimilation system. Comparison of the operational model SIT data to all  
25 available observations (in situ and satellite) showed that the TOPAZ4 reanalysis reproduces the  
26 observed seasonal cycle and the rates of advance and melting of SIT in the ESS, with average bias  
27 of approximately  $\pm 20$  cm. Pattern correlation analysis of the SIT forecast data over 4 years  
28 (2013–2016) reveals that the early summer SIT distribution is skillfully predicted for a lead time of  
29 up to 3 days, but that the prediction skill drops abruptly after the 4th day, which is related to  
30 dynamical process controlled by synoptic-scale atmospheric fluctuations. For longer lead times ( $>4$   
31 days), the thermodynamic melting process takes over, which makes most of the remaining prediction  
32 skill. In July 2014, during which an ice-blocking incident occurred, relatively thick SIT ( $\sim 150$  cm)  
33 was simulated over the ESS, which is consistent with the reduction of vessel speed. These results  
34 suggest that TOPAZ4 sea ice information has a great potential for practical applications in  
35 summertime maritime navigation via the NSR.

36



## 37 **1 Introduction**

38 During recent decades, sea ice cover in the Northern Hemisphere has shown remarkable  
39 reduction and the largest rates of decrease of  $100,000 \text{ km}^2 \text{ decade}^{-1}$  has been observed in the western  
40 Arctic Ocean in summer [Cavalieri and Parkinson, 2008]. Sea ice retreat influences the light  
41 conditions for phytoplankton photosynthesis activity [Wassmann, 2011], and the resultant meltwater  
42 influences the marine environment via ocean acidification [Yamamoto-Kawai et al., 2011]. In winter,  
43 shrinkage of the sea ice area in marginal seas, such as the Barents Sea changes the surface boundary  
44 conditions of the atmosphere, influences planetary waves, and causes blocking events that are one of  
45 the possible causes of the recent severe winters in mid-latitude regions [Honda et al., 2009; Inoue et  
46 al., 2012; Mori et al., 2014; Overland et al., 2015; Petoukhov and Semenov, 2010; Screen, 2017].

47 In contrast to these climatic consequences and problems for the marine ecosystem caused by the  
48 reduction in sea ice, the retreat of Arctic sea ice has new opportunities for commercial maritime  
49 navigation. It has been reported that exploitation of shipping routes in the Arctic Ocean, i.e., the  
50 Northern Sea Route (NSR), could reduce the navigational distance between Europe and Asia by about  
51 40% in comparison with routes via the Suez Canal [Schøyen and Bråthen, 2011]. Melia et al. [2016]  
52 discussed the possibility of a viable trans-Arctic shipping route in the 21st century, based on the  
53 Coupled Model Intercomparison Project Phase 5 global climate model simulation. Currently, the  
54 summertime use of the NSR by commercial vessels such as cargo ships and tankers has increased  
55 [Eguíluz et al., 2016]. Therefore, obtaining precise information on sea ice condition and evaluating  
56 the forecast skill of operational sea ice models have become urgent issues.

57 Many previous studies have examined the predictability of summertime sea ice change in the  
58 Arctic Ocean in terms of its coverage [Wang et al., 2013] and motion [Schweiger and Zhang, 2015].  
59 Kimura et al. [2013] reported a good correlation of the spatial distribution of summertime sea ice  
60 concentration (SIC) with winter ice divergence/convergence. Their study indicated that sea ice  
61 thickness (SIT) or sea ice volume before the melt season is a source of predictability for summertime



62 SIC. Recently, their study was supported by hindcast experiments undertaken using a climate model,  
63 in which the SIC in the East Siberian Sea (ESS) was shown to have significant seasonal prediction  
64 skill [Bushuk et al., 2017]. The significant impacts of SIT condition on the seasonal prediction of SIC  
65 in the Arctic Ocean have been highlighted by many studies [Lindsay et al., 2008; Holland et al., 2011;  
66 Blanchard-Wrigglesworth and Bitz, 2014; Collow et al., 2015; Melia et al., 2015; Chen et al. 2017;  
67 Melia et al. 2017]. Thus, the persistence of SIT or sea ice volume is one of the key factors determining  
68 the skill of seasonal predictions of summertime sea ice area.

69 Earlier studies have focused primarily on the seasonal to interannual predictability of SIC or sea  
70 ice area in the Arctic Ocean; thus, subseasonal variation in SIT and its predictability have not been  
71 examined fully for near-term route planning. Although the summertime sea ice extent has rapidly  
72 decreased on interannual timescale, substantial sea ice area still remains in critical stretches of the  
73 NSR such as the ESS in early summer (June–July). Since precise information regarding SIT and its  
74 near-future condition is crucial for icebreaker operations [Tan et al., 2013; Pastusiak, 2016], it is  
75 important to clarify the medium-range (3 to 10 days lead time) predictability of summertime SIT in  
76 the Arctic Ocean.

77 Synoptic-scale fluctuations of cyclone and anticyclone is greater over the Arctic Ocean and  
78 Eurasia in summer than in winter [Serreze and Barry, 1988; Serreze and Barrett, 2008]. In recent  
79 years, there is a risk that an Arctic cyclone becomes extremely developed and covered the entire  
80 Pacific sector [Simmonds and Rudeva, 2012; Yamagami et al. 2017]. Because the ESS corresponds  
81 to the route of Arctic cyclones generated over the Eurasian Continent [Orsolini and Sorteberg, 2009],  
82 it is expected that synoptic-scale atmospheric fluctuations would influence substantially the spatial  
83 distribution of SIT and ice motion in the ESS. Ono et al. [2016] highlighted the importance of  
84 atmospheric prediction skill on medium-range forecasts of sea ice distribution in the ESS based on a  
85 case of an extreme cyclone that occurred on 6 August 2012. On the other hand, earlier studies pointed  
86 out that the sea ice melting process is important for the long-term prediction of summertime sea ice



87 extent [e.g., Bushuk et al., 2017]. But the relative importance of dynamical and thermodynamic  
88 processes on the medium-range forecast skill of summertime sea ice properties has not yet been well  
89 understood.

90 Since 2010, ice–ocean forecasts and a 20-years reanalysis are available for the Arctic Ocean,  
91 based on the TOPAZ ocean data assimilation system (Towards an Operational Prediction system for  
92 the North Atlantic European coastal Zones) in its 4th version [Sakov et al., 2012]. The Norwegian  
93 Meteorological Institute provides 10-day forecast products in daily mean fields, forced at the surface  
94 by the ECMWF operational atmospheric forecasts, updated daily and distributed by the Copernicus  
95 Marine Environment Monitoring Services (<http://marine.copernicus.eu>). The reliability of the  
96 corresponding TOPAZ4 reanalysis data has been evaluated previously through comparison with in  
97 situ and satellite SIT data [Xie et al. 2017; Nakanowatari et al. 2017]. They showed the SIT in the  
98 TOPAZ4 reanalysis data are comparable to observed values over the Beaufort Gyre and central Arctic  
99 Ocean, although the SIT overall shows a negative bias of several dozen centimeters throughout a year.  
100 Thus, it is expected that the SIT data in the TOPAZ reanalysis data should also be reliable in the ESS  
101 even in the melting season, and the forecast SIT data should show skillful prediction skill on medium-  
102 range time scale.

103 In this study, we examined the predictability of the early summer SIT distribution in the ESS on  
104 the medium-range timescale and discussed its underlying physical mechanisms, based on the  
105 TOPAZ4 forecast dataset and trivial dynamical and thermodynamical models. Section 2 describes  
106 the data and methods. Section 3 evaluates the reliability of the SIT data in the TOPAZ4 reanalysis  
107 data through comparison with all available in situ and satellite observations, as well as operational  
108 model analyses, with particular emphasis on the ESS. In section 4, we examine the predictability of  
109 the SIT distribution in the ESS based on TOPAZ4 forecast data. Section 5 examines the relationship  
110 between sea ice conditions and vessel speed during an ice-blocking event that occurred in July 2014.  
111 A discussion and the derived conclusions are presented in section 6.



112

## 113 **2 Data and Methods**

114 This study used daily mean sea ice data derived from the TOPAZ4 Arctic sea ice forecast system  
115 dataset, in which the SSM/I SIC data, hydrographic temperature and salinity data, along-track sea  
116 level anomaly, and satellite estimates of ice drift and sea surface temperature were assimilated, but  
117 sea ice thickness was not yet assimilated in this version of the reanalysis [Simonsen et al. 2017]. The  
118 TOPAZ4 system was designed as a regional ice–ocean coupled system forced with atmospheric flux  
119 data. The ocean model of TOPAZ4 is based on version 2.2 of HYCOM, which uses isopycnal  
120 vertical coordinates in the ocean interior and z level coordinates in the near-surface layer. The sea ice  
121 model uses an elastic–viscous–plastic rheology [Hunke and Dukowicz, 1997]. The thermodynamic  
122 processes are based on a three-layer thermodynamic model with one snow and 2 ice layers [Semtner,  
123 1976] with a modification for subgrid-scale ice thickness heterogeneities [Fichefet and Morales  
124 Maqueda, 1997]. The model domain covers the Arctic Ocean and the North Atlantic, and the lateral  
125 boundaries are relaxed to monthly mean climatological data. The spatial resolution is 12–16 km with  
126 28 hybrid layers, which constitutes eddy-permitting resolution in low- and mid-latitude regions but  
127 not in the Arctic Ocean. It has been reported that the SIT of the TOPAZ4 reanalysis data has  
128 substantial negative bias from 2001 to 2010 due to excessive snowfall, which has been modified after  
129 2011 [Xie et al., 2017]. Therefore, this study used SIT data from 1 January 2011 to 31 December  
130 2014.

131 The data assimilation method of TOPAZ4 is a deterministic version of the ensemble Kalman  
132 filter (EnKF) [Sakov and Oke, 2008] with an ensemble of 100 dynamical members. Since EnKFs  
133 have time-dependent state error covariances, this method is suitable for data assimilation of  
134 anisotropic variables in areas close to the sea ice edge [Lisæter et al. 2003, Sakov et al. 2012]. In this  
135 system, in situ hydrographic observations are assimilated together with satellite observations of the  
136 ocean such as sea surface temperature and sea surface height. Since this system assimilates the SIC



137 and sea ice velocity (but the latter only in cold season), one should expect adequate simulation of SIT  
138 through the ridging process [Stark et al. 2008]. The TOPAZ4 reanalysis data were produced forced  
139 with 6-hourly atmospheric fluxes from the ERA Interim reanalysis [Dee et al., 2011]. The surface  
140 turbulent heat flux and momentum flux were both calculated using bulk formula parameterizations  
141 [Kara et al., 2000; Large and Pond, 1981]; thus, fluxes derived from the atmospheric model were not  
142 used. The forecast and reanalysis systems have almost the same settings and their results are similar  
143 during their overlap period (not shown).

144 To evaluate the prediction skill of the TOPAZ4 forecast system, we used daily mean sea ice  
145 forecast data from 2012 to 2016 [Simonsen et al. 2017]. A probabilistic 10-member ensemble forecast  
146 was performed with the ECMWF medium-range (up to 10 days) atmospheric forecast data updated  
147 daily, out of which only the ensemble average is used. We excluded the forecast data of 2012 in this  
148 study, because the sea ice coverage of the ESS in early summer was quite small. Since the forecast  
149 data were only provided weekly before 2016, the total of 259 cases was assembled during the study  
150 period. The skill core was quantified using pattern correlation coefficients (PCCs), which are used  
151 widely in deterministic forecast verification [Barnett and Schlesinger, 1987]:

$$152 \quad PCC = \frac{\sum_{ij=1}^N (f_{ij} - \bar{f}_{ij})(a_{ij} - \bar{a}_{ij})}{\sqrt{\sum_{ij=1}^N (f_{ij} - \bar{f}_{ij})^2} \sqrt{\sum_{ij=1}^N (a_{ij} - \bar{a}_{ij})^2}} \quad (1)$$

153 where  $f_{ij}$  and  $a_{ij}$  are forecast and analysis sea ice variables, respectively. The overbar denotes the  
154 average values over the analyzed area (see Fig. 1a); thus the PCC reflects the correlation of observed  
155 and signal anomalies relative to their respective spatial means.

156 To evaluate the reliability of the SIT values in the TOPAZ4 reanalysis data during the freezing  
157 season, we mainly used the merged product of CryoSat-2 (CS2) and the Soil Moisture and Ocean  
158 Salinity (SMOS) SIT products (hereafter, CS2SMOS) from 2011 to 2014 [Ricker et al. 2017], which  
159 were provided by the online sea-ice data platform “meereisportal.de” [Grosfeld et al. 2016]. These



160 data are interpolated to 25-km resolution based on optimal interpolation and they are available from  
161 October to April. In general, CS2 data have large uncertainty in the estimation of SIT of <1 m, while  
162 the SMOS relative uncertainties are lowest for very thin ice. Thus, the merged product is – to date –  
163 considered the best estimate of the SIT distribution across the entire Arctic Ocean, including the ESS.

164 For the melting season (May–July), there is no reliable estimate of SIT distribution in the ESS,  
165 we therefore used only in situ SIT data of autonomous ice mass balance (IMB) buoys obtained  
166 between 26 March and 29 July 2014 near the ESS [Perovich et al., 2013]. To compare the two-  
167 dimensional SIT data with IMB buoy data, we re-gridded the gridded SIT data along the IMB buoy  
168 trajectories. This comparison method is almost identical to that adopted by Sato and Inoue [2017]  
169 who compared IMB buoy data with SIT data of the NCEP-CFSR reanalysis. As a reference for SIC,  
170 we used daily mean SIC data derived from AMSR2 passive microwave radiometer sensors using the  
171 bootstrap algorithm [Comiso and Nishio, 2008; JAXA, 2013].

172 As an alternative model reanalysis, we used the PIOMAS outputs, which are derived from the  
173 coupled ice–ocean modeling and assimilation system based on the Parallel Ocean Program POP and  
174 the Thickness and Enthalpy Distribution (TED) sea ice model, forced with NCEP-NCAR reanalysis  
175 data [Zhang et al., 2003]. In this dataset, SIC and sea surface temperature are assimilated by adoptive  
176 nudging, and many studies [Schweiger et al., 2011; Lindsay and Zhang, 2006; Stroeve et al., 2014]  
177 have compared PIOMAS output with observed SIT data and found it the most reliable estimate of  
178 observed SIT in the Arctic Ocean [Laxon et al., 2013; Wang et al. 2016]. The temporal and horizontal  
179 resolutions of the observed and simulated SIT data are summarized in Table 1. Before comparing the  
180 gridded SIT data with IMB buoy data in each grid point, we reconstructed these SIT data on a 0.25°  
181 latitude–longitude grid by applying bilinear interpolation.

182 To examine the source of medium-range predictability in SIT distribution, we also used  
183 ECMWF atmospheric forecast data on a 1.25° latitude–longitude grid from 2013 to 2016, derived  
184 from the THORPEX Interactive Grand Global Ensemble through its data portal



185 (<http://tigge.ecmwf.int>). This dataset is very similar to the atmospheric forecast data used for the  
186 TOPAZ4 operational forecast system [Simonsen et al. 2017]. For the examination of atmospheric  
187 forecast skill, we used 51 ensemble daily means of zonal and meridional wind speed at 10-m height  
188 on the same days for the TOPAZ4 forecast data at lead times of 0–10 day.

189 To evaluate the influence of sea ice condition on vessel speed in the ESS, we used Automatic  
190 Identification System (AIS) data from two tankers during their passage through the ESS on 4–26 July  
191 2014, which were provided by Shipfinder (<http://jp.shipfinder.com/>). Their ice classes correspond to  
192 IA Super in the Finnish–Swedish Ice Class Rules, and these vessels are capable of navigating sea ice  
193 regions in which SIT is up to 50–90 cm. Both tankers were likely to be hindered considerably by ice  
194 conditions, even under escort by Russian nuclear-powered ice-breakers; thus, these AIS data are  
195 considered suitable for a case study of the influence of SIT on icebreaker speed.

196

### 197 **3 Comparisons between TOPAZ4 and other available SIT data**

198 Figure 1a shows the spatial distribution of observed (CS2SMOS) SIT in April (when SIT is  
199 maximum) in the Arctic marginal seas of the Laptev Sea, ESS, and Chukchi sea. The sea ice  
200 observations show the maximum thickness (>3 m) near Greenland, but relatively thick ice (~1.8 m)  
201 can also be found around the ESS. These features are qualitatively simulated in the TOPAZ4  
202 reanalysis data (Fig. 1b). The differences in SIT between the TOPAZ4 reanalysis and CS2SMOS data  
203 reveal remarkable negative bias (i.e., smaller than –0.8 m) in the TOPAZ4 reanalysis in the central  
204 Arctic Ocean (Fig. 1c); however, the magnitude of the negative bias is smaller in coastal areas such  
205 as the ESS. The PCC of SIT between TOPAZ4 and CS2SMOS in the Arctic marginal seas (65°–80°N,  
206 80°E–160°W, shown in Fig. 1a) is 0.89 in April, which is comparable with that between the PIOMAS  
207 output and CS2SMOS (Table 2). The PCCs in other months are also comparable with those of the  
208 PIOMAS output. It should be noted that a larger positive bias in TOPAZ4 is located solely in the  
209 region of the Beaufort Gyre, with about 50 cm excess thickness (Fig. 1c). This positive bias is



210 however consistent with the large underestimation of CS2SMOS SIT over the Beaufort Sea, which is  
211 related to the existence of heavily deformed ice [Ricker et al. 2017].

212 Figure 2 shows the time series of daily mean SIT derived from CS2SMOS, TOPAZ4 reanalysis,  
213 and PIOMAS output, averaged over the ESS (70°–80° N, 150°–180° E, shown in Fig. 1a). The  
214 TOPAZ4 SIT data are reasonably similar to the seasonal cycle of CS2SMOS data with maxima in  
215 April–May and minima in October–November, although the TOPAZ4 SIT data at the beginning of  
216 2011 are highly underestimated. This might be related to the persistence of the negative bias until  
217 2010 [Xie et al., 2017]. The monthly mean biases of TOPAZ4 SIT data relative to CS2SMOS are less  
218 than –23 cm in March and April (Table 3). Thus, even though the negative bias in the TOPAZ4  
219 reanalysis data is relatively large in the central Arctic (Fig. 1c), the TOPAZ4 SIT is comparable with,  
220 or larger than, the CS2SMOS data over the Arctic marginal seas. The PIOMAS SIT also follows the  
221 seasonal cycle of CS2SMOS data, but it is overestimated somewhat from January to May (Fig. 2).  
222 The mean biases of PIOMAS SIT relative to CS2SMOS are 48 and 66 cm in March and April,  
223 respectively, which are much larger than for TOPAZ4 (Table 3). In the melting season (May–July),  
224 the seasonal reduction in SIT of TOPAZ4 near the ESS is comparable with that observed in the IMB  
225 buoy data (Fig. 3). The TOPAZ4 SIT has weak positive bias of <25 cm relative to the IMB buoy data  
226 from May to July (Table 3), which is smaller than for PIOMAS. Consequently, the TOPAZ4 SIT in  
227 the ESS can be considered successful in simulating the seasonal cycles of CS2SMOS and IMB buoy  
228 data within the range of approximately  $\pm 20$  cm, which is lower than the negative bias found in the  
229 central Arctic Ocean. The errors in the central Arctic Ocean and Beaufort Sea are probably larger  
230 because they contain older multi-year ice for which the SIT errors have accumulated errors in sea ice  
231 drift and thermodynamics over longer times.

232



#### 233 **4. Medium-range forecast skill of SIT distribution in the ESS**

234 In this section, we evaluate the prediction skill of SIT based on the PCCs between the analysis  
235 and predicted data in the ESS. However, before this evaluation, we examine the mean fields and the  
236 variability of the SIT and SIC distributions in early summer. Figure 4a presents the spatial distribution  
237 of the climatological SIT and SIC in July, which shows that relatively thick sea ice (~1 m) covers  
238 50%–70% of the ESS. Along the zone of the sea ice edge, the temporal standard deviation of the daily  
239 mean SIT anomaly is relatively large with the maximum value of 0.6 m in the coastal region (Fig.  
240 4b) and the area-averaged value is maximum in July–August (Fig. 4c). Since the SIT reduction rate  
241 in the ESS is strongest in these months (Fig. 4c) and the storm activity is prevalent for periods of  
242 several days [Orsolini and Sorteberg, 2009], it is likely that dynamical and thermodynamically-  
243 induced SIT variations are large. Note that the RMS of the SIC anomaly averaged over the ESS also  
244 shows a similar seasonal cycle (not shown). Thus, it is meaningful to examine the medium-range  
245 predictability of early summer SIT distribution in the ESS.

246 Figure 5 shows the seasonal dependency of PCC between the predicted and analyzed SIT at lead  
247 times of 0–9 days. We found that the overall prediction skill is relatively low in June–July with a  
248 larger spread compared with the cold season (January–May), which is consistent with the larger  
249 variance of the SIT anomaly in the ESS (Fig. 4c). In early summer (June–July), the SIT distribution  
250 is predicted skillfully for a lead time of up to 3 days (Fig. 6); however, the prediction skill decreases  
251 abruptly at a lead time of 4 days, in which the standard deviation is also relatively large. Since such  
252 an abrupt reduction of the prediction skill is also found in May and October (Fig. 5), when the  
253 influence of sea ice melt is quite small (Fig. 4c), the abrupt reduction of early summer SIT prediction  
254 skill might be attributable to dynamical advection of sea ice.

255 To examine the influence of dynamical processes on the prediction skill of early summer SIT  
256 distribution, we consider the prediction skill of sea ice velocities and surface wind velocities. The  
257 prediction skill of sea ice velocity stays on a high level (~0.8) with small spread for a lead time of up



258 to 3 days, but decreases down to 0.6–0.7 for a lead time of 4 days (Fig. 7a). The early summer  
259 prediction skill of surface wind speed also shows the same abrupt decrease at a lead time of 4 days,  
260 and the rate of decrease of prediction skill is larger in meridional direction (Fig. 7b). Since the SIT  
261 distribution has a zonally homogeneous pattern (Fig. 4a), it is suggested that the meridional  
262 component of SIT advection is sensitive to the sea ice transport, which influences the SIT distribution  
263 in the ESS. These results confirm that the prediction skills of the sea ice velocities are strongly related  
264 to those of surface wind speeds in the ESS.

265 Figure 8 shows the temporal evolutions of SIT and ice velocity for analysis and a forecast  
266 bulletin starting from 2nd July 2015, which is a typical case of the abrupt decrease in the prediction  
267 skill of SIT as well as sea ice velocities for a lead time of 4 days (Fig. 8; lower panel). For lead times  
268 of +0 (2 July) to +2 days (4 July), the spatial distributions of SIT and ice velocity are predicted  
269 skillfully with only small differences between them (Fig. 8; right panels). At a lead time of +4 days  
270 (6 July), the analyzed sea ice velocity is directed northwestward in the ESS, which is related to the  
271 cyclonic circulation over the Novosibirsk Islands; however, the predicted sea ice velocity is directed  
272 southwestward. At a lead time of +6 days, the predicted and analyzed sea ice velocity are completely  
273 unrelated. The resultant southward anomaly of sea ice velocity leads to positive and negative  
274 anomalies in SIT in the coastal and offshore regions, respectively. We also examined the time  
275 evolutions of the surface wind velocities in the atmospheric forecast data, and found them very similar  
276 to the sea ice velocity fields (not shown). These results indicate that the abrupt reduction of the  
277 prediction skill of early summer SIT in the ESS is related to a deficiency at predicting Arctic cyclone.

278 Further, we examine diagnostically the ice drift speed and direction based on a classical free-  
279 drift theory [Leppäranta, 2005], using the sea ice speed of TOPAZ4 reanalysis data and ERA interim  
280 atmospheric wind data in July 2011–2014. The general solution of sea ice speed ( $u$ ) can be described  
281 as complex numbers:



282 
$$u = \alpha e^{-i\theta} U_a + U_{wg}, \quad (2)$$

283 where  $U_a$ , and  $U_{wg}$  are the wind speed and geostrophic water velocities, respectively. The terms  $\alpha$  and  
284  $\theta$  are the wind factor and the deviation angle of ice motion from the surface wind, respectively, where  
285 a positive angle is in counterclockwise direction. If we neglect the geostrophic water velocity  $U_{wg}$ ,  
286 the wind factor and deviation angle can be obtained in the following form:

287 
$$\alpha^4 + 2 \sin \theta_w R N a \alpha^3 + R^2 N a^2 \alpha^2 - N a^4 = 0, \quad (3)$$

288 
$$\theta = \arctan \left( \tan \theta_w + \frac{R N a}{\alpha \cos \theta_w} \right) - \theta_a, \quad (4)$$

289 where  $\theta_w$  and  $\theta_a$  are the boundary layer turning angles of water and air, respectively. The turning angle  
290  $\theta$  is the angle between the vectors of the ice–water stress and the sea ice motion, which is a  
291 consequence of the viscous effect within the ocean boundary layer. The Nansen number  $Na$  is defined  
292 by  $\sqrt{\rho_a C_a / \rho_w C_w}$ , where  $\rho_a$  and  $\rho_w$  represent the density of air and water, respectively, and  $C_a$  and  
293  $C_w$  are air and water drag coefficients, respectively. The Rossby number  $R$  is defined by  
294  $(\rho h_{ice} f) / (\rho_w C_w N a |U_a|)$ , where  $\rho$  is the ice density,  $f$  is the Coriolis parameter, and  $|U_a|$  is the speed  
295 of the surface wind. To calculate the wind factor  $\alpha$  and the deviation angle  $\theta$  under a given surface  
296 wind speed, we used constant parameters of  $C_a = 1.2 \times 10^{-3}$ ,  $C_w = 5 \times 10^{-3}$ ,  $\rho_a = 1.3 \text{ kg m}^{-3}$ ,  $\rho_w =$   
297  $1026 \text{ kg m}^{-3}$ ,  $\rho = 910 \text{ kg m}^{-3}$ ,  $f = 1.3 \times 10^{-4} \text{ s}^{-1}$ , and  $\theta_w = 20^\circ$ , which are values typical of the Arctic  
298 Ocean [McPhee, 2012]. The value of  $\alpha$  was calculated numerically from a 4th-order polynomial (Eq.  
299 (3)).

300 On a first order approximation, the daily mean sea ice speed is linearly proportional to the surface  
301 wind speed (10-m height) averaged over a part of the ESS (Fig. 9a). The correlation between them is  
302 0.96, which is significant at the 99% confidence level, based on the Monte Carlo simulation [Kaplan  
303 and Glass, 1995]. The regression coefficient of ice speed onto the 10-m wind speed is 0.022, which



304 is consistent with the well-known 2% relationship between the speed of ice and the surface wind  
305 speed [Thorndike and Colony, 1982]. The number of the TOPAZ4 ice speed data within  $\pm 20\%$  of the  
306 theoretical value is 79 days, which accounts for 63% of the total analyzed period. Note that the  
307 observed regression coefficient is somewhat larger than the theoretical value (0.018) averaged over  
308 the range of surface wind speed of  $2\text{--}10\text{ m s}^{-1}$  calculated from Eq. (2). Since the classical free drift  
309 theory [Leppäranta, 2005] neglects both the Ekman layer velocity and the ocean geostrophic velocity,  
310 the absence of an ice-ocean boundary layer is likely to underestimate the wind-induced ice velocity  
311 [Park and Stewart, 2016]. The deviation angle of sea ice motion in TOPAZ4 is estimated as  $20^\circ\text{--}40^\circ$   
312 under a wind condition  $>5\text{ cm s}^{-1}$ , but it gradually increases to  $40^\circ\text{--}70^\circ$  under weaker wind conditions  
313 of  $<5\text{ cm s}^{-1}$  (Fig. 9b). The decrease of the deviation angle as the surface wind strengthens is also  
314 consistent with earlier studies [Thorndike and Colony, 1982]. These observed deviation angles are  
315 comparable with their theoretical values calculated using Eq. (4). The finding that the estimated  
316 values of the wind factor and the deviation angle are approximately within the range of typical surface  
317 wind parameters (i.e., 2% for the wind factor and  $30^\circ$  for the deviation angle) in the Arctic Ocean  
318 confirms that sea ice velocity in the ESS is controlled predominantly by wind stress drag: thus, the  
319 influence of ocean currents is not essential.

320 It is interesting that the prediction skill of SIT in early summer remains at high level after the  
321 lead time of 4 days (Fig. 6), despite the poorer prediction skill of sea ice velocity (Fig. 7a). This  
322 suggests that the SIT prediction skill after a lead time of 4 days is not attributed to the dynamical  
323 process but rather the thermodynamic process (i.e., the melting process of sea ice). To evaluate the  
324 effect of sea ice melting on SIT prediction skill, we roughly estimated the thermodynamic SIT change  
325 based on a simple sea ice melting model, as follows:

326 
$$h^p(t) = h^a(t_0) + \Delta t \times \overline{dh} / dt, \quad (5)$$



327 where  $h^p$  is the predicted thermodynamic SIT change,  $h_i^a$  is the initial condition, which is derived  
328 from the analysis SIT, and  $\overline{dh}/dt$  is the rate of reduction of SIT due to sea ice melting. It is known  
329 that the summertime surface heat flux in the Pacific sector of the Arctic Ocean is dominated by the  
330 shortwave radiation flux [Perovich et al. 2007; Steele et al. 2008]. Recently, the seasonal evolution  
331 of sea ice retreat in early summer has been found to be explained well by a simplified ice–ocean  
332 coupled model, in which shortwave radiation is assumed constant [Kashiwase et al. 2017]. Therefore,  
333 as the melting rate of the SIT in each year, we used the reduction rate of SIT calculated from the  
334 climatological analysis SIT data during 2013–2016, which is likely to reflect the typical  
335 thermodynamic melting rate in recent years and the SIT change due to transient sea ice advection  
336 seems to be negligible. Here, we also evaluate the prediction skill of the persistency in the initial SIT  
337 in the ESS (first term of the RHS in Eq. (5)).

338 Figure 10 shows the prediction skills of early summer SIT in the simple sea ice melting and  
339 persistency models. The prediction skill of the simple melting model, which is lower than the full  
340 physics model, is very similar to that of the persistency model up to 3 days. However, the prediction  
341 skill of the simple melting model is comparable with that of the full physics model after a lead time  
342 of 4 days, which is higher than that of persistency. Figure 11 shows the temporal evolutions of SIT  
343 difference between the forecast and analysis data in each prediction model in the period 2–9 July  
344 2015. From the lower panel of Fig. 11, we found that the prediction skill of the full physics model is  
345 higher than the simple melting and persistency models for lead times of 0–5 days, but comparable  
346 with the prediction skill of the simple melting model at longer lead times (> 6 days). In the SIT  
347 difference map of the full-physics model minus the operational analysis, a positive anomaly (i.e.,  
348 overestimation of SIT), is evident along the sea ice edge at a lead time of 4 days, and then gradually  
349 increases until a lead time of 8 days. For the case of the simple melting model, a similar positive  
350 anomaly emerges at a lead time of 4 days, but the positive anomaly appears stationary along the



351 coastal region, compared to the full physics model. The persistency model overestimates SIT over  
352 the entire region during the prediction. These results support the idea that the melting process is  
353 important in the prediction of early summer SIT over longer timescales. Looking back at the seasonal  
354 dependency of SIT prediction skill (Fig. 5), the loss of prediction skills past the 4th day in  
355 December–February appear larger than in June–August. The difference in prediction skill between  
356 lead times of 4 day and 9 day, averaged in January–February, is 0.05, which is somewhat larger than  
357 in June–July (0.03). This result implies that the wintertime SIT prediction skill without any  
358 thermodynamic melting process is largely controlled by the weak skill of atmospheric prediction, and  
359 thus indirectly supports the assertion that the extension of the skillful prediction of early summer SIT  
360 is attributable to the thermodynamic melting process.

361

### 362 **5. Case study of ice-blocked incident in the ESS in July 2014**

363 In the perspective of operational application of the TOPAZ4 sea ice data to the maritime  
364 navigation of the NSR, we briefly examine the relationship between the sea ice conditions and AIS  
365 vessel speed data for the case of an ice-blocking incident involving two vessels, based on the TOPAZ4  
366 reanalysis data. Figure 13 shows the vessel tracks during July 4–30 2014, when the two vessels  
367 became blocked in the ESS for about one week. During this period, SIT in excess of 100 cm is found  
368 in the ESS with the maximum thickness of 150 cm. A joint statistical analysis of the daily mean SIT  
369 in the TOPAZ4 reanalysis and the vessel speed along the route indicates that vessel speed is  
370 significantly anticorrelated with SIT ( $-0.80$ ) during the entire passage (Fig. 14a), significant at the  
371 95 % confidence level based on a Monte Carlo technique [Kaplan and Glass, 1995]. The correlation  
372 between the SIC and vessel speed is also significant ( $r=-0.77$ ), although the absolute value of the  
373 correlation coefficient is lower than for SIT. This result suggests that vessel speed was influenced by  
374 sea ice stress due to SIT and indirectly supports the reliability of the daily mean SIT of the TOPAZ4  
375 reanalysis data in the ESS in early summer.



376

## 377 **6. Summary and discussion**

378 In this study, the medium-range forecast skill of early summer SIT distribution in the ESS was  
379 evaluated using the TOPAZ4 data assimilation system. Comparisons between the observed,  
380 operational model, and TOPAZ4 reanalysis SIT data showed that the TOPAZ4 reanalysis reproduces  
381 the observed seasonal variation (maximum in April–May and minimum in October–November)  
382 including the rates of advance and melting of sea ice in the ESS. Earlier studies have identified that  
383 the SIT of the TOPAZ4 reanalysis data is underestimated, even in the ESS, but the negative bias  
384 relative to the in situ and satellite observations was about 20 cm from winter to summer, which is  
385 smaller than another reliable hindcast model output (PIOMAS). Thus, the TOPAZ4 SIT data could  
386 be considered reliable estimates for the ESS even in the absence of satellite observations in summer.

387 The prediction skill of the SIT distribution in the TOPAZ4 forecast system was examined in the  
388 ESS using a pattern correlation analysis. Although the prediction skill was relatively lower in early  
389 summer (June–July) with a large spread, the SIT distribution was predicted skillfully for a lead time  
390 of up to 3 days, and the prediction skill drops abruptly after the 4th day. A similar change in prediction  
391 skill was also found for sea ice velocity and surface wind speed over the ESS. Diagnostic analysis of  
392 the sea ice velocity variability revealed that the early summer ice speed and direction over the EES  
393 could be explained well by the free-drift mechanism with a wind factor of 2.2 % and a deviation angle  
394 of 30°–50°. These results suggested that the large reduction of prediction skill could be attributed to  
395 the process of dynamical advection of sea ice; thus, the prediction of early summer SIT distribution  
396 will depend on precise prediction of the surface wind. Our comprehensive analysis supports an earlier  
397 study that suggested the dynamical processes have an essential role in the prediction skill of sea ice  
398 distribution on short timescales [Ono et al., 2016].

399 The time evolution of SIT and the related ice velocity relates the large difference between the  
400 forecast and analysis data at a lead time of 4 days to the low forecast skills for an Arctic cyclone event.



401 Jung and Matsueda [2017] highlighted that large-scale atmospheric fluctuations in the Arctic region  
402 in winter are predicted skillfully for lead times of up to 5 days in the operational forecast system,  
403 which is very similar to the prediction skill in mid-latitude regions. However, Yamagami et al. [2018]  
404 reported that the skillful prediction of Arctic cyclones generated in summer is limited to 4 days, which  
405 is shorter than the case for the mid-latitudes [Froude, 2010]. As this area is located near the transit  
406 zone of summertime storm tracks generated over Eurasia [Serreze and Barry, 1988], the predictability  
407 of Arctic cyclones could be an important factor in the determination of the lead time of surface wind  
408 speed and thus, of the SIT distribution in the ESS. The low prediction skill of the meridional wind  
409 and ice speed suggested that the meridional component of sea ice advection contributes substantially  
410 to the SIT distribution in the ESS. Since it was reported that additional radiosonde observations over  
411 the Arctic Ocean have considerable impact on the prediction skill in synoptic-scale fluctuations  
412 [Inoue et al., 2015; Yamazaki et al., 2015], additional radiosonde observations acquired over the  
413 Arctic Ocean could lead to further extension of the lead time for medium-range forecast skill of SIT  
414 distribution.

415 It is interesting that the prediction skill of early summer SIT remains at a high level after a lead  
416 time longer than 4 days in spite of the poor prediction skill of the sea ice velocity and surface wind  
417 fields. Based on sensitivity experiments using a simple melting and a persistency model, it was found  
418 that the longer timescale prediction of SIT in early summer could be attributed to the thermodynamic  
419 melting process. As the shortwave radiation flux is maximum in early summer (June–July), the  
420 change of SIT due to the advection in relation to synoptic-scale atmospheric fluctuations is likely to  
421 be smaller than the thermodynamic SIT reduction along the sea ice edge. Although the recognition of  
422 the importance of the thermodynamic melting process on sea ice prediction on seasonal timescales  
423 has been pointed out by earlier studies [Kimura et al. 2012; Bushuk et al. 2017; Kashiwase et al.  
424 2017], our study clarified that the influence has a substantial role on the medium-range forecast of  
425 early summer SIT distribution. Thus, the influence of sea ice advection on early summer sea ice



426 prediction is limited to a lead time of 4–5 days, but is dominated by the thermodynamic melting  
427 process in later stage of the lead times. In other words, the SIT prediction skill in early summer is not  
428 necessarily worse at the longer timescale. It is noteworthy that the dynamical process is not  
429 unimportant for the long-term prediction in the SIT distribution in early summer, because the skillful  
430 prediction skill at a lead time of 3 days is important as the initial conditions for the melting process  
431 dominated for a lead time longer than 4 days. Thus, it is concluded that the atmospheric prediction  
432 skill for a lead time of up to 3 days contributes to the short and medium-range prediction skill of the  
433 SIT distribution in early summer.

434 In view of the operational application of the TOPAZ4 sea ice data to the navigation in NSR, this  
435 study found that during an ice-blocking event that affected two tankers in the ESS in July 2014,  
436 significant SIT (~150 cm) was simulated over the ESS by TOPAZ4. Given that the SIT is found to be  
437 underestimated by 20 cm in TOPAZ4, the true SIT is expected to be above 150 cm. Statistical analysis  
438 suggested that vessel speed was highly anticorrelated with the daily mean SIT variations (–0.80)  
439 rather than the SIC (–0.77). This result demonstrated the reliability of the early summer SIT  
440 distribution in the TOPAZ4 reanalysis data and its high potential for operational use in support of  
441 maritime navigation of the NSR. However, this result was only based on a case study of two ships in  
442 July 2014. To clarify the determinant factor on vessel speed, comprehensive statistical analysis will  
443 be needed based on the speed data of different types of vessel.

444 Future projections for storm track activity (intensity and number) under the scenario of Arctic  
445 climate change have been addressed by several researchers. For example, based on control  
446 experiments using climate models, Bengtsson et al. [2006] found that summertime storm activity is  
447 expected to increase. Orsolini and Sorteberg [2009] found that the number of storms, particularly  
448 along the Eurasian Arctic coast, could increase in the future, because of the local enhancement of the  
449 meridional temperature gradient between the Arctic Ocean and the warmed Eurasian continent. Nishii  
450 et al. [2015] supported that their findings based on analyses using the Coupled Model Intercomparison



451 Project (CMIP) -3 and -5, although they highlighted that the CMIP projections had considerable  
452 uncertainty. Thus, further investigations of the formation and the development mechanisms of  
453 summertime Arctic cyclones are needed for the improvement of the prediction skill of atmospheric  
454 wind conditions, which are responsible for the forecast skill of early summer sea ice distribution over  
455 4 days.  
456



457 **Acknowledgements**

458 The AMSR2 brightness temperatures and products data were provided by the Japan Aerospace  
459 Exploration Agency (JAXA). The dataset of AMSR2 SIT and SIC was archived and provided by the  
460 Arctic Data archive System (ADS), which was developed by the National Institute of Polar Research  
461 (NIPR). The merging of CryoSat-2 und SMOS data was funded by the ESA project SMOS+ Sea Ice  
462 (4000101476/10/NL/CT and 4000112022/14/I-AM) and data from 2010 to 2014 were obtained from  
463 <http://www.meereisportal.de> (Grant No.: REKLIM-2013-04). The ECMWF atmospheric forecast  
464 data were provided by the ECMWF TIGGE portal site via the TIGGE medium of the University of  
465 Tsukuba (<http://gpvjma.ccs.hpcc.jp/TIGGE/>). The TOPAZ4 forecast data were analyzed using the  
466 Pan-Okhotsk Information System of ILTS. This work was funded by the Arctic Challenge for  
467 Sustainability (ArCS) project of the Ministry of Education, Culture, Sports, Science and Technology  
468 in Japan. We thank James Buxton MSc from Edanz Group ([www.edanzediting.com/ac](http://www.edanzediting.com/ac)) for correcting  
469 a draft of this manuscript.

470



471 **References**

- 472 Barnett T. P., & Schlesinger M. E. 1987. Detecting changes in global climate induced by greenhouse  
473 gases. *J. Geophys. Res.* 92, 14772–14780, doi:10.1029/JD092iD12p14772.
- 474 Bengtsson L., Hodges K.I., & Roeckner E. 2006. Storm Tracks and Climate Change. *J. Climate* 19,  
475 3518–3543, <https://doi.org/10.1175/JCLI3815.1>.
- 476 Blanchard-Wrigglesworth E. & Bitz, C. M. 2014. Characteristics of Arctic Sea-Ice Thickness  
477 Variability in GCMs. *J. Climate* 27, 8244–8258.
- 478 Bushuk M., Msadek R., Winton M., Vecchi G. A., Gudgel R., Rosati A., & Yang X. 2017. Skillful  
479 regional prediction of Arctic sea ice on seasonal timescales. *Geophys. Res. Lett.* 44,  
480 doi:10.1002/2017GL073155.
- 481 Cavalieri D. J. & Parkinson C. L. 2008. Arctic sea ice variability and trends, 1979–2006. *J. Geophys.*  
482 *Res.* 113, C07003, doi:10.1029/2007JC004558.
- 483 Chen Z., Liu J., Song M., Yang Q., & Xu S. 2017. Impacts of Assimilating Satellite Sea Ice  
484 Concentration and Thickness on Arctic Sea Ice Prediction in the NCEP Climate Forecast System.  
485 *J. Climate* 30, 8429–8446.
- 486 Collow T., Wang W., Kumar A., & Zhang J. 2015. Improving Arctic Sea Ice Prediction Using  
487 PIOMAS Initial Sea Ice Thickness in a Coupled Ocean–Atmosphere Model. *Mon. Wea. Rev.*  
488 143, 4618–4630, doi: 10.1175/MWR-D-15-0097.1.
- 489 Comiso J. C. 2012. Large Decadal Decline of the Arctic Multiyear Ice Cover. *J. Climate* 25, 1176–  
490 1193, <https://doi.org/10.1175/JCLI-D-11-00113.1>.
- 491 Dee D. P. et al. 2011. The ERA-Interim reanalysis: configuration and performance of the data  
492 assimilation system. *Q.J.R. Meteorol. Soc.* 137, 553–597. doi: 10.1002/qj.828.
- 493 Eguíluz V. M., Fernández-Gracia J., Irigoien X., & Duarte C. M. 2016. A quantitative assessment of  
494 Arctic shipping in 2010–2014. *Sci. Rep.* 6, 30682, doi:10.1038/srep30682.
- 495 Fichet T., & Maqueda M. A. M. 1997. Sensitivity of a global sea ice model to the treatment of ice



- 496 thermodynamics and dynamics. *J. Geophys. Res.* 102, 12609–12646, doi:10.1029/97JC00480.
- 497 Froude L. S. R. 2010. TIGGE: Comparison of the prediction of Northern Hemisphere extratropical  
498 cyclones by different ensemble prediction systems. *Weather and Forecasting* 25, 819–836.  
499 <https://doi.org/10.1175/2010WAF2222326.1>.
- 500 Grosfeld K., Treffeisen R., Asseng J., Bartsch A., Bräuer B., Fritsch B., Gerdes R., Hendricks S.,  
501 Hiller W., Heygster G., Krumpen T., Lemke P., Melsheimer C., Nicolaus M., Ricker R., &  
502 Weigelt M. 2016. Online sea-ice knowledge and data platform <[www.meereisportal.de](http://www.meereisportal.de)>,  
503 Polarforschung, Bremerhaven, Alfred Wegener Institute for Polar and Marine Research &  
504 German Society of Polar Research 85, 143-155, doi:10.2312/polfor.2016.011.
- 505 Holland M. M., Bailey, D. A. & Vavrus, S. 2011. Inherent sea ice predictability in the rapidly  
506 changing Arctic environment of the Community Climate System Model, version 3. *Clim. Dyn.*  
507 36, 1239–1253, doi:10.1007/s00382-010-0792-4.
- 508 Honda M., Inoue J., & Yamane S. 2009. Influence of low Arctic sea-ice minima on anomalously cold  
509 Eurasian winters. *Geophys. Res. Lett.* 36, L08707, doi:10.1029/2008GL037079.
- 510 Hunke E. & Dukowicz J. 1997. An Elastic–Viscous–Plastic Model for Sea Ice Dynamics. *J. Phys.*  
511 *Oceanogr.* 27, 1849–1867.
- 512 Inoue J., Hori M., & Takaya K. 2012. The role of Barents sea ice in the wintertime cyclone track and  
513 emergence of a Warm-Arctic Cold Siberian anomaly. *J. Climate* 25, 2561-2568.
- 514 Inoue J., Yamazaki A., Ono J., Dethloff K., Maturilli M., Neuber R., Edwards P., & Yamaguchi H.  
515 2015. Additional Arctic observations improve weather and sea-ice forecasts for the Northern  
516 Sea Route. *Sci. Rep.* 5, 16868, doi:10.1038/srep1686.
- 517 JAXA 2013. Descriptions of GCOM-W1 AMSR2 Level 1R and Level 2 Algorithms, Rev. A.
- 518 Jung, T. & Matsueda, M. 2016. Verification of global numerical weather forecasting systems in polar  
519 regions using TIGGE data. *Q.J.R. Meteorol. Soc.* 142: 574–582. doi: 10.1002/qj.2437.
- 520 Kaplan, D. & Glass L. 1995. *Understanding nonlinear dynamics*, Springer-Verlag, New York, pp.



- 521 420.
- 522 Kara A., Rochford P., & Hurlburt H. 2000. Efficient and Accurate Bulk Parameterizations of Air–  
523 Sea Fluxes for Use in General Circulation Models. *J. Atmos. Oceanic Technol.* 17, 1421–1438.
- 524 Kashiwase H., Ohshima K. I., Nihashi S., & Eicken H. 2017. Evidence for ice-ocean albedo feedback  
525 in the Arctic Ocean shifting to a seasonal ice zone. *Sci. Rep.* 7, 8170, doi:10.1038/s41598-017-  
526 08467-z.
- 527 Kimura N., Nishimura A., Tanaka Y., & Yamaguchi H. 2013. Influence of winter sea-ice motion on  
528 summer ice cover in the Arctic. *Polar Research* 1751-8369,  
529 doi:<http://dx.doi.org/10.3402/polar.v32i0.20193>.
- 530 Large W.G. & Pond S. 1981. Open Ocean Momentum Flux Measurements in Moderate to Strong  
531 Winds. *J. Phys. Oceanogr.* 11, 324–336.
- 532 Laxon S. W., Giles K. A., Ridout A. L., Wingham D. J., Willatt R., Cullen R., Kwok R., Schweiger  
533 A., Zhang J., Haas C., Hendricks S., Krishfield R., Kurtz N., Farrell S. & Davidson M. 2013.  
534 CryoSat-2 estimates of Arctic sea ice thickness and volume, *Geophys. Res. Lett.* 40, 732–737.
- 535 Leppäranta M. 2005. *The Drift of Sea Ice*. Springer-Verlang, 266 pp.
- 536 Lisæter K. A., Rosanova J., & Evensen G. 2003. Assimilation of ice concentration in a coupled ice-  
537 ocean model, using the Ensemble Kalman filter. *Ocean Dynamics* 53, 368–388.  
538 <http://doi.org/10.1007/s10236-003-0049-4>.
- 539 Lindsay R.W. & Zhang J. 2006. Arctic Ocean Ice Thickness: Modes of Variability and the Best  
540 Locations from Which to Monitor Them. *J. Phys. Oceanogr.* 36, 496–506,  
541 <https://doi.org/10.1175/JPO2861.1>.
- 542 Lindsay R. W., Zhang J., Schweiger A. J., & Steele M. A. 2008. Seasonal predictions of ice extent in  
543 the Arctic Ocean. *J. Geophys. Res.* 113, C02023, doi:10.1029/2007JC004259.
- 544 McPhee M. G. 2012. Advances in understanding ice-ocean stress during and since AIDJEX. *Cold  
545 Reg. Sci. Technol.* 76, 24-36.



- 546 Melia N., Haines K., & Hawkins E. 2015. Improved Arctic sea ice thickness projections using bias-  
547 corrected CMIP5 simulations. *The Cryosphere* 9, 2237-2251, doi:10.5194/tc-9-2237-2015.
- 548 Melia N., Haines K., & Hawkins E. 2016. Sea ice decline and 21st century trans-Arctic shipping  
549 routes. *Geophys. Res. Lett.* 43, 9720–9728, doi:10.1002/2016GL069315.
- 550 Melia N., Haines K., Hawkins E., & Day J. J. 2017. Towards seasonal Arctic shipping route  
551 predictions. *Env. Res. Lett.* 12, 084005.
- 552 Mori M., Watanabe M., Shiogama H., Inoue J., & Kimoto M. 2014. Robust Arctic sea-ice influence  
553 on the frequent Eurasian cold winters in past decades. *Nat. Geosci.*, **7**, 869–873.
- 554 Nakanowatari T., Sato K., & Inoue J. 2014. Predictability of the Barents Sea Ice in Early Winter:  
555 Remote Effects of Oceanic and Atmospheric Thermal Conditions from the North Atlantic. *J.*  
556 *Climate* 27, 8884–8901, doi: 10.1175/JCLI-D-14-00125.1.
- 557 Nishii K., Nakamura H., Orsolini Y. J. 2015. Arctic summer storm track in CMIP3/5 climate models.  
558 *Clim. Dyn.*, 44, 1311, <https://doi.org/10.1007/s00382-014-2229-y>.
- 559 Ono J., Inoue J., Yamazaki A., Dethloff K., & Yamaguchi H. 2016. The impact of radiosonde data  
560 on forecasting sea-ice distribution along the Northern Sea Route during an extremely developed  
561 cyclone. *J. Adv. Model Earth Syst.* 8, 292-303, doi:10.1002/2015MS000552.
- 562 Orsolini Y. J. & Sorteberg A. 2009. Projected changes in Eurasian and Arctic summer cyclones under  
563 global warming in the Bergen climate model. *Atmos. Oceanic Sci. Lett.* 2, 62-67.
- 564 Overland J. E., Francis J. A., Hall R., Hanna E., Kim S.-J., & Vihma T. 2015. The melting Arctic and  
565 mid-latitude weather patterns: Are they connected? *J. Climate*, 28, 7917-7932,  
566 doi:10.1175/JCLI-D-14-00822.1.
- 567 Park H.-S. & Stewart A. L. 2016. An analytical model for wind-driven Arctic summer sea ice drift,  
568 *The Cryosphere*, 10, 227–244.
- 569 Pastusiak T. 2016. *The Northern sea route as a shipping lane*. Springer, Switzerland, p. 219.
- 570 Perovich D. K., Light B., Eicken H., Jones K. F., Runcimen K., & Nghiem S. V. 2007. Increasing



- 571 solar heating of the Arctic Ocean and adjacent seas, 1979–2005: Attribution and the role of ice-  
572 albedo feedback. *Geophys. Res. Lett.* 34, L19505, doi:10.1029/2007GL031480.
- 573 Perovich D., Richter-Menge J., Elder B., Arbetter T., Claffey K., & Polashenski C. 2013. Observing  
574 and understanding climate change: Monitoring the mass balance, motion, and thickness of Arctic  
575 sea ice. Cold Regions Research and Engineering Laboratory. [http://www.imb-crrel-](http://www.imb-crrel-dartmouth.org/imb.creel)  
576 [dartmouth.org/imb.creel](http://www.imb-crrel-dartmouth.org/imb.creel).
- 577 Persson A. 2011. User guide to ECMWF forecast products ver. 1.2, October 2011, ECMWF, Reading,  
578 pp. 121.
- 579 Petoukhov V., & Semenov V. A. 2010. A link between reduced Barents-Kara sea ice and cold winter  
580 extremes over northern continents. *J. Geophys. Res.* 115, D21111, doi:10.1029/2009JD013568.
- 581 Ricker R., Hendricks S., Kaleschke L., Tian-Kunze X., King J., & Haas C. 2017. A weekly Arctic  
582 sea-ice thickness data record from merged CryoSat-2 and SMOS satellite data. *The Cryosphere*  
583 11, 1607-1623, <https://doi.org/10.5194/tc-11-1607-2017>.
- 584 Sakov P., & Oke P. R. 2008. A deterministic formulation of the ensemble Kalman filter: an alternative  
585 to ensemble square root filters. *Tellus* 60A, 361–371.
- 586 Sakov P., Counillon F., Bertino L., Lisæter K. A., Oke P. R., & Korablev A. 2012. TOPAZ4: an  
587 ocean-sea ice data assimilation system for the North Atlantic and Arctic. *Ocean Sci.* 8, 633-656,  
588 doi:10.5194/os-8-633-2012.
- 589 Sato K. & Inoue J. 2017. Comparison of Arctic sea ice thickness and snow depth estimates from  
590 CFSR with in situ observations. *Clim. Dyn.* 1-13, doi:10.1007/s00382-017-3607-z.
- 591 Schøyen H., & Bråthen S. 2011. The Northern Sea route versus the Suez Canal: cases from bulk  
592 shipping. *J. Transp. Geogr.* 19, 977–983.
- 593 Screen J. A. 2017. Simulated Atmospheric Response to Regional and Pan-Arctic Sea Ice Loss. *J.*  
594 *Climate* 30, 3945–3962, <https://doi.org/10.1175/JCLI-D-16-0197.1>
- 595 Schweiger A., Lindsay R., Zhang J., Steele M., Stern H., & Kwok R. 2011. Uncertainty in modeled



- 596 Arctic sea ice volume. *J. Geophys. Res.* 116, C00D06, doi:10.1029/2011JC007084.
- 597 Schweiger A. J., & Zhang J. 2015. Accuracy of short-term sea ice drift forecasts using a coupled ice-  
598 ocean model. *J. Geophys. Res. Oceans* 120, 7827–7841, doi:10.1002/2015JC011273.
- 599 Semtner A. 1976. A Model for the Thermodynamic Growth of Sea Ice in Numerical Investigations  
600 of Climate. *J. Phys. Oceanogr.* 6, 379–389.
- 601 Serreze M. C. & Barry R. G. 1988. Synoptic activity in the Arctic basin, 1979–85. *J. Climate* 1,  
602 1276–1295.
- 603 Serreze M. C. & Barrett A. P. 2008. The summer cyclone maximum over the central Arctic Ocean. *J.*  
604 *Climate* 21, 1048–1065.
- 605 Simonsen M., Hackett B., Bertino L., Røed L. P., Waagbø G. A., Drivdal M., Sutherland G. 2017.  
606 PRODUCT USER MANUAL For Arctic Ocean Physical and Bio Analysis and Forecasting  
607 Products 5.5. EU, Copernicus Marine Service, <http://marine.copernicus.eu> pp. 56.
- 608 Simmonds I. & Rudeva I. 2012. The great Arctic cyclone of August 2012. *Geophys. Res. Lett.* 39,  
609 L23709, <https://doi.org/10.1029/2012GL054259>.
- 610 Stark J. D., Ridley J., Martin M., & Hines A. 2008. Sea ice concentration and motion assimilation in  
611 a sea ice–ocean model. *J. Geophys. Res.* 113, C05S91, doi:10.1029/2007JC004224.
- 612 Steele M. Ermold W., & Zhang J. 2008. Arctic Ocean surface warming trends over the past 100 years.  
613 *Geophys. Res. Lett.* 35, L02614, doi:10.1029/2007GL031651.
- 614 Stroeve J., Hamilton L. C., Bitz C. M., & Blanchard-Wrigglesworth E. 2014. Predicting September  
615 sea ice: Ensemble skill of the SEARCH Sea Ice Outlook 2008–2013. *Geophys. Res. Lett.* 41,  
616 2411–2418, doi:10.1002/2014GL059388.
- 617 Tan X., Su K., Riska K., & Moan T. 2013. A six-degrees-of-freedom numerical model for level ice–  
618 ship interaction. *Cold Reg. Sci. Technol.* 92, 1–16, doi:10.1016/j.coldregions.2013.03.006.
- 619 Thorndike A. S. & Colony R. 1982. Sea ice motion in response to geostrophic winds. *J. Geophys.*  
620 *Res.* 87, 5845–5852, doi:10.1029/JC087iC08p05845.



- 621 Wang W., Chen M., & Kumar A. 2013. Seasonal Prediction of Arctic Sea Ice Extent from a Coupled  
622 Dynamical Forecast System. *Mon. Wea. Rev.* 141, 1375–1394, doi: 10.1175/MWR-D-12-  
623 00057.1.
- 624 Wang X., Key J., Kwok R., & Zhang J. 2016. Comparison of Arctic Sea ice thickness from satellites,  
625 aircraft, and PIOMAS data. *Remote Sens.* 8, 713, doi:10.3390/rs8090713.
- 626 Wassmann P. 2011. Arctic marine ecosystems in an era of rapid climate change. *Prog. Oceanogr.* 90,  
627 1–17.
- 628 Xie J., Bertino L., Counillon F., Lisæter K. A., & Sakov P. 2017. Quality assessment of the TOPAZ4  
629 reanalysis in the Arctic over the period 1991–2013. *Ocean Sci.* 13, 123–144, doi:10.5194/os-13-  
630 123-2017.
- 631 Yamagami A., Matsueda M., & Tanaka H. L. 2017. Extreme Arctic cyclone in August 2016. *Atmosph.*  
632 *Sci. Lett.* 18: 307–314. doi: 10.1002/asl.757.
- 633 Yamagami A., Matsueda M., & Tanaka H. L. 2018. Predictability of the 2012 great Arctic cyclone  
634 on medium-range timescales, *Polar Sci.* (in press).
- 635 Yamamoto-Kawai M., McLaughlin F. A., & Carmack E. C. 2011. Effects of ocean acidification,  
636 warming and melting of sea ice on aragonite saturation of the Canada Basin surface water.  
637 *Geophys. Res. Lett.* 38, L03601, doi:10.1029/2010GL045501.
- 638 Yamazaki A., Inoue J., Dethloff K., Maturilli M., & König-Langlo G. 2015. Impact of radiosonde  
639 observations on forecasting summertime Arctic cyclone formation. *J. Geophys. Res.* 120, 3249–  
640 3273, doi:10.1002/2014JD022925.
- 641 Zhang J. & Rothrock D. A. 2003. Modeling global sea ice with a thickness and enthalpy distribution  
642 model in generalized curvilinear coordinates. *Mon. Wea. Rev.* 131, 681–697.
- 643



644 **Table 1.** List of observed and simulated sea ice thickness datasets

Data sources		Period	Spatial resolution	Time step
TOPAZ4	Reanalysis	2011–2014	12.5 km	Daily
	Forecast	2013–2016	12.5 km	Daily
CS2SMOS		2011–2014 (October to April)	~25 km	7 days
IMB		26 March to 29 July 2014	Point-wise	Hourly
PIOMAS		2011–2014	~0.8°	Daily

645

646 **Table 2.** Pattern correlations between monthly mean climatologies of SIT in CS2SMOS, and the  
 647 TOPAZ4 and PIOMAS models over the Arctic marginal seas (Laptev, East Siberian, and Chukchi  
 648 Seas)

Month	Jan.	Feb.	Mar.	Apr.	Oct.	Nov.	Dec.
TOPAZ4	0.97	0.96	0.93	0.89	0.97	0.98	0.97
PIOMAS	0.97	0.95	0.92	0.90	0.98	0.98	0.97

649

650 **Table 3.** Monthly mean SIT biases relative to observed SIT averaged over the ESS

SIT bias (cm)	CS2SMOS (2011–2014)		IMB (2014)		
	Mar.	Apr.	May	Jun.	Jul.
TOPAZ4	-23	<1	25	17	<1
PIOMAS	48	66	47	28	37

651

652



653 **Figure captions**

654 **Figure 1.** Spatial distribution of climatological monthly mean of SIT (cm) in April during 2011–  
655 2014: (a) CS2SMOS, (b) TOPAZ4 reanalysis, and (c) their difference (cm). The boundaries of the  
656 ESS and Arctic marginal seas are indicated in panel (a) by thick and thin lines, respectively.

657 **Figure 2.** Time series of daily mean SIT (cm) averaged over the ESS (rectangular region denoted by  
658 black line in Fig. 1 (a)) derived from CS2SMOS (black), TOPAZ4 reanalysis (red), and PIOMAS  
659 (blue) from January 2011 to August 2014. For CS2SMOS data, 7 day mean values are shown.

660 **Figure 3.** The IMB trajectory near the ESS from 26 March to 29 July 2014. (a) Spatial distribution  
661 of daily mean SIC (%) in the AMSR2 on 29 July 2014. (b) Time series of SIT (cm) of IMB (black),  
662 TOPAZ4 reanalysis (red), and PIOMAS (blue) along the IMB buoy trajectory (shown in panel a).

663 **Figure 4.** Spatial distribution of (a) monthly mean (colors) climatological SIT (m) in the TOPAZ4  
664 reanalysis and (b) the RMS variability of daily mean SIT (colors) in July during 2011–2014. The  
665 monthly mean of climatological SIC (white contours) in July is indicated in panel (a). The rectangular  
666 region enclosing the ESS (70°–80°N, 150°–180°E) is shown in panel (b). (c) Time series of monthly  
667 mean SIT (grey shade) and RMS of TOPAZ4 reanalysis (black line) averaged over the ESS. The  
668 scale of the RMS is indicated on the right axis.

669 **Figure 5.** The PCCs (colors) between operational forecast and analysis SIT in the ESS (70°–80°N,  
670 150°–180°E) in each month, averaged from 2013–2016. The isoline of standard deviation of the  
671 PCCs at 0.05 is shown with white contours.

672 **Figure 6.** PCCs between forecast and analysis SIT from operational TOPAZ4 data in early summer  
673 (June–July) averaged on 2013–2016. Error bar indicates the standard deviation of the PCCs.

674 **Figure 7.** The PCCs between forecast and analysis (a) zonal (black) and meridional ice speed (red)  
675 and (b) zonal (black) and meridional (red) surface wind speed in June–July averaged from 2013–2016.  
676 Error bar indicates the standard deviation of the PCCs.



677 **Figure 8.** Temporal evolution of SIT (cm; colors) and ice velocity ( $\text{m s}^{-1}$ ; vectors) distribution for  
678 (left) analysis, (center) forecast, and (right) the difference between forecast and analysis at increasing  
679 lead times from +0 day to +6 days initialized on 2nd July 2015. The corresponding PCCs for the SIT  
680 (black), zonal (red) and meridional ice speeds (blue) in the ESS (right-lower panel of the time  
681 evolution) are shown in the lower panel. The scale for the PCCs of the zonal and meridional ice  
682 speeds is indicated on the right axis.

683 **Figure 9.** (a) Relationship between 10m wind speed ( $\text{m s}^{-1}$ ) in the ERA Interim reanalysis data and  
684 sea ice speed ( $\text{m s}^{-1}$ ) in the TOPAZ4 reanalysis averaged over a part of the ESS ( $72^{\circ}$ – $76^{\circ}$  N,  
685  $150^{\circ}$ – $170^{\circ}$  E) during 1–31 July 2011–2014. Broken and solid lines indicate the regression line of ice  
686 speed on 10m wind speed ( $y = 0.0224x - 0.0112$ ) and the theoretical ice speed estimated based on  
687 classical free-drift theory, respectively. (b) Angle (degrees) of sea ice velocity relative to surface wind  
688 vectors averaged over the ESS. Positive values indicate sea ice drift is to the right of the wind direction.  
689 Solid curve indicates the wind–ice velocity angle estimated based on classical free-drift theory.

690 **Figure 10.** The PCCs between forecast and analysis SIT from the full physics model (black),  
691 persistency (red), and a simple melting model (blue) in July averaged from 2013–2016. Error bar  
692 indicates the standard deviation of the PCCs.

693 **Figure 11.** Temporal evolution of SIT differences (cm; colors) between the forecast and analysis data  
694 at lead times increasing from +2 to +8 days, initialized on 2nd July 2015. In each panel, the sea ice  
695 edge of the analysis, defined by 30% SIC, is shown. Corresponding PCCs for the full physics model  
696 (black), a simple melting model (red) and persistency (blue) in the ESS (right-lower panel of the time  
697 evolution) are shown in the lower panel.

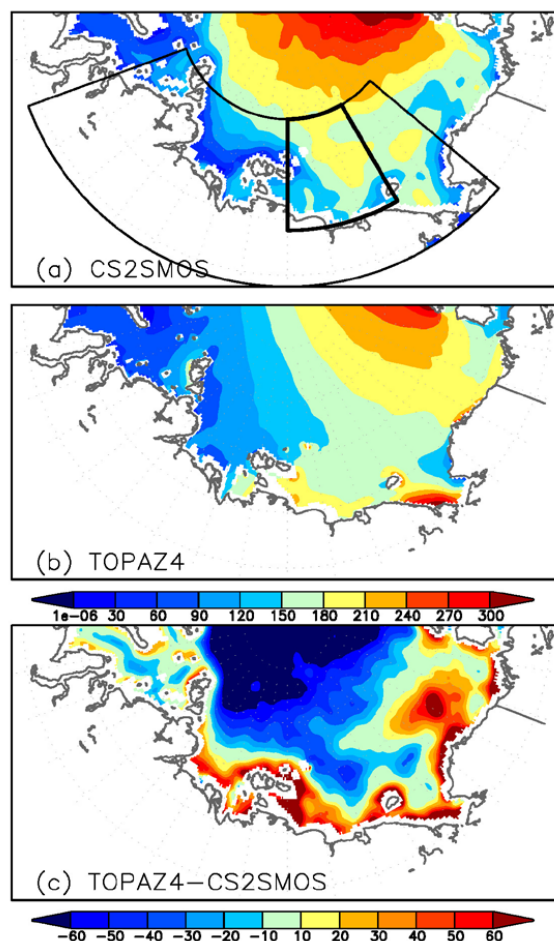
698 **Figure 12.** Trajectory of the two tankers over the ESS based on AIS data. The routes cross the ESS  
699 from the Laptev Sea on 4 July 2014 to the port of Yamal on 31 July 2014, via the port of Pevek on  
700 20 July 2014. The forward route is highlighted by green circles. The SIT (cm; colors) and SIC (%;  
701 contours) averaged over the period of the forward route are shown.



702 **Figure 13.** Scatter plots of daily mean vessel speeds (knots) and sea ice thickness (cm) from 4–30  
703 July 2014.

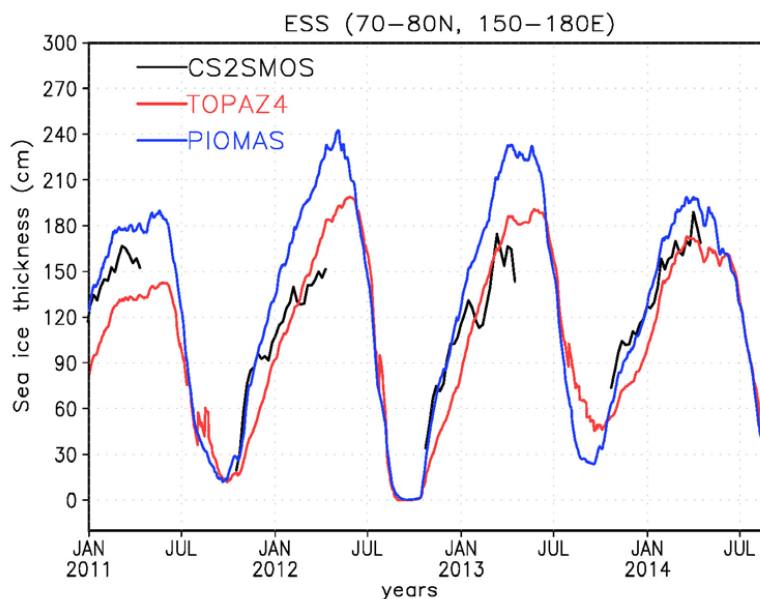


704



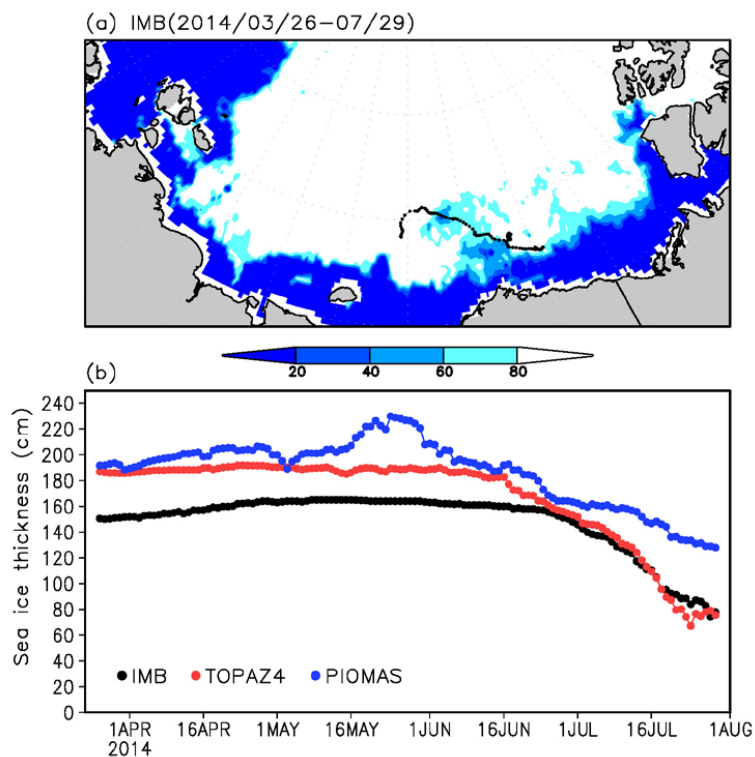
705

706 **Figure 1.** Spatial distribution of climatological monthly mean of SIT (cm) in April during 2011–  
707 2014: (a) CS2SMOS, (b) TOPAZ4 reanalysis, and (c) their difference (cm). The boundaries of the  
708 ESS and Arctic marginal seas are indicated in panel (a) by thick and thin lines, respectively.



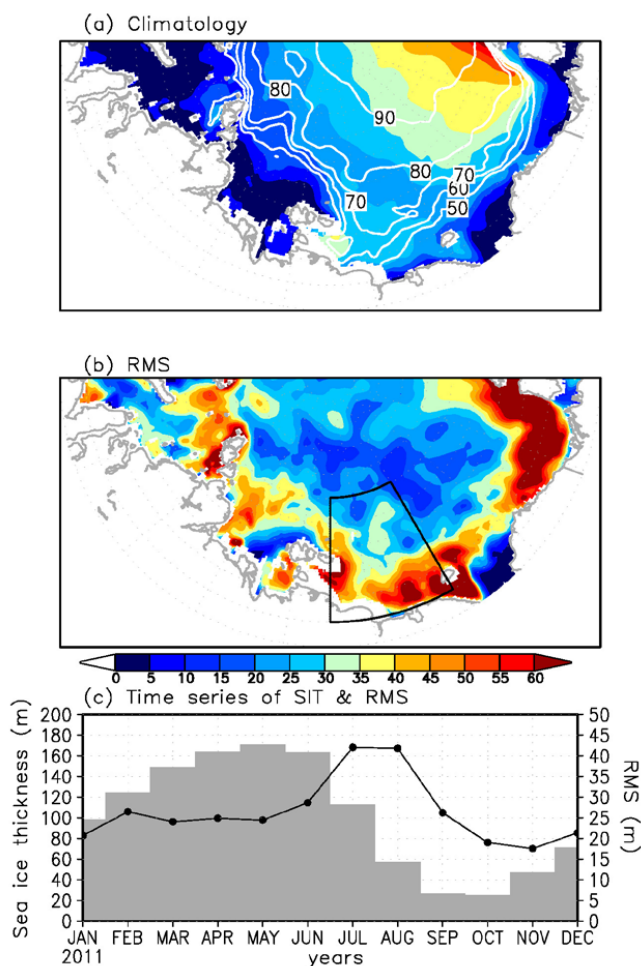
709

710 **Figure 2.** Time series of daily mean SIT (cm) averaged over the ESS (rectangular region denoted by  
711 black line in Fig. 1 (a)) derived from CS2SMOS (black), TOPAZ4 reanalysis (red), and PIOMAS  
712 (blue) from January 2011 to August 2014. For CS2SMOS data, 7 day mean values are shown.



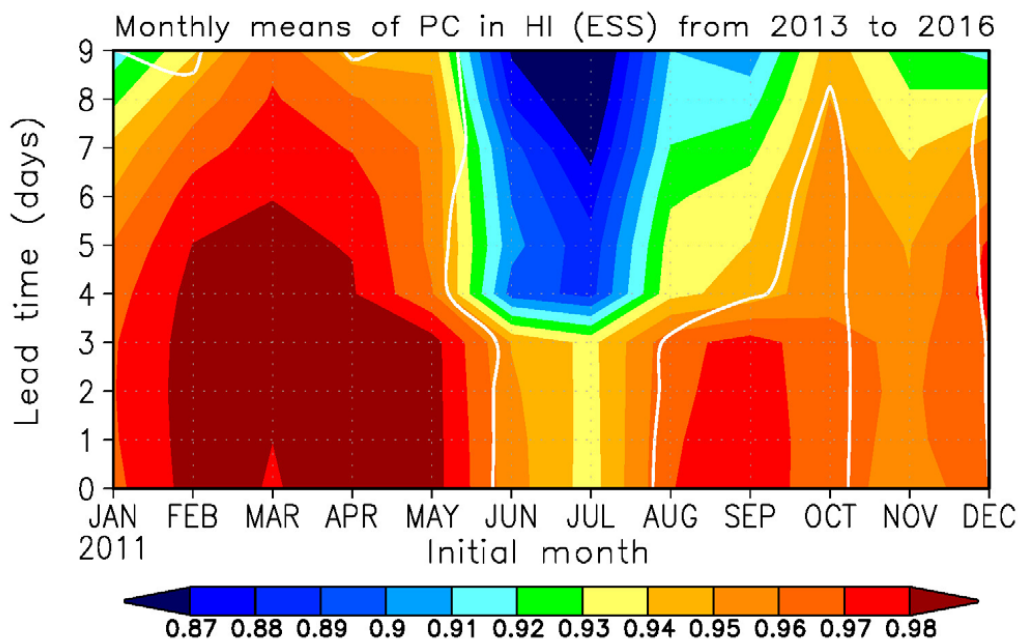
713

714 **Figure 3.** The IMB trajectory near the ESS from 26 March to 29 July 2014. (a) Spatial distribution  
715 of daily mean SIC (%) in the AMSR2 on 29 July 2014. (b) Time series of SIT (cm) of IMB (black),  
716 TOPAZ4 reanalysis (red), and PIOMAS (blue) along the IMB buoy trajectory (shown in panel a).



717

718 **Figure 4.** Spatial distribution of (a) monthly mean (colors) climatological SIT (m) in the TOPAZ4  
 719 reanalysis and (b) the RMS variability of daily mean SIT (colors) in July during 2011–2014. The  
 720 monthly mean of climatological SIC (white contours) in July is indicated in panel (a). The rectangular  
 721 region enclosing the ESS (70°–80°N, 150°–180°E) is shown in panel (b). (c) Time series of monthly  
 722 mean SIT (grey shade) and RMS of TOPAZ4 reanalysis (black line) averaged over the ESS. The  
 723 scale of the RMS is indicated on the right axis.



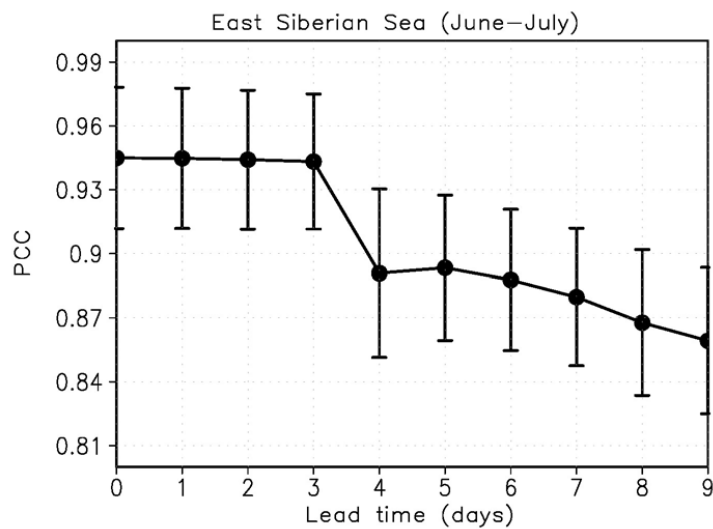
724

725 **Figure 5.** The PCCs (colors) between operational forecast and analysis SIT in the ESS (70°–80°N,

726 150°–180°E) in each month, averaged from 2013–2016. The isoline of standard deviation of the

727 PCCs at 0.05 is shown with white contours.

728

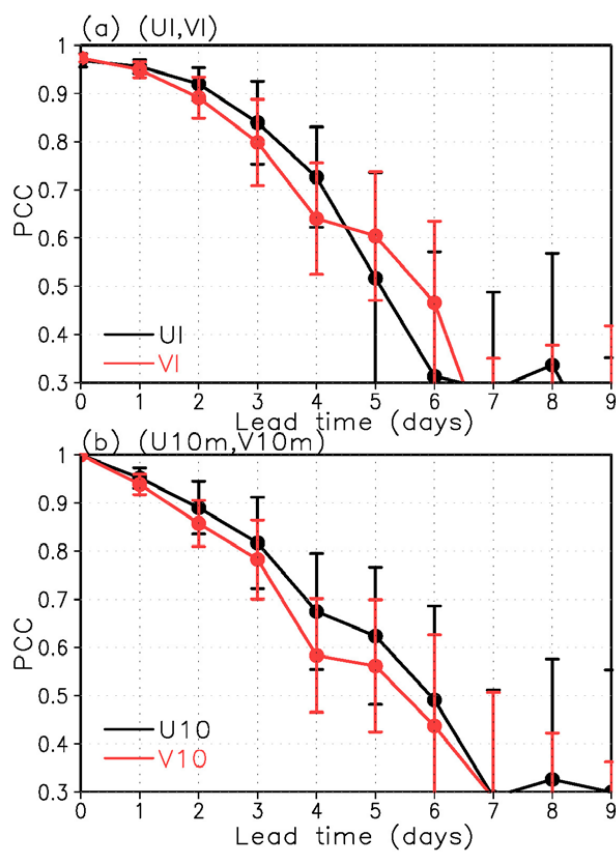


729

730 **Figure 6.** PCCs between forecast and analysis SIT from operational TOPAZ4 data in early summer

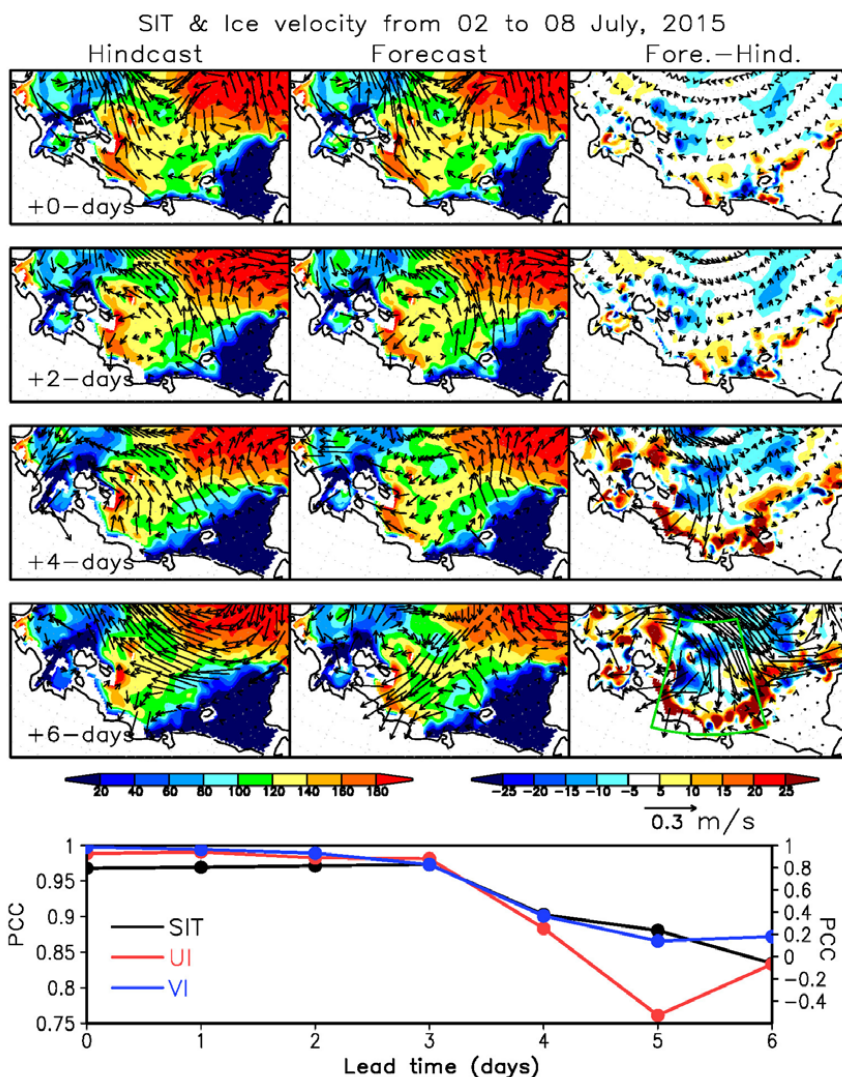
731 (June–July) averaged on 2013–2016. Error bar indicates the standard deviation of the PCCs.

732

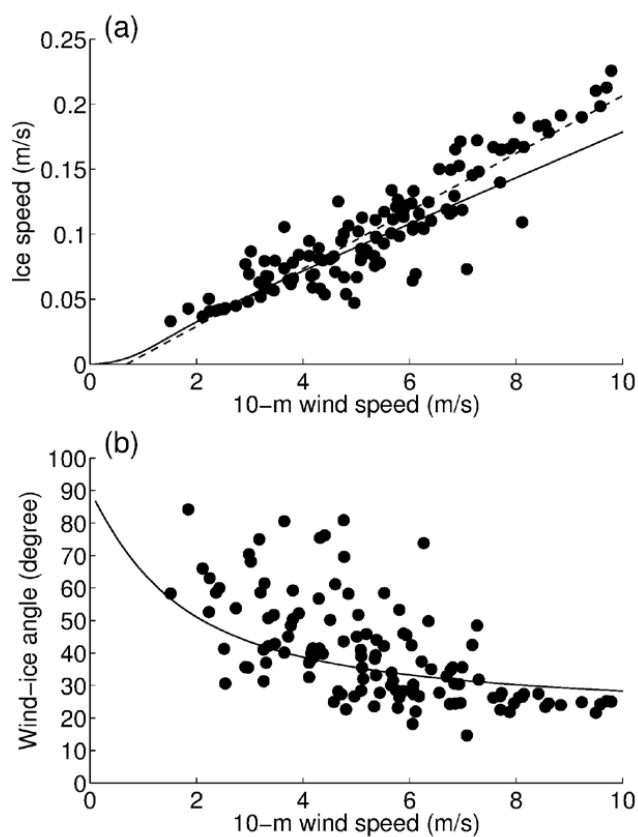


733

734 **Figure 7.** The PCCs between forecast and analysis (a) zonal (black) and meridional ice speed (red)  
735 and (b) zonal (black) and meridional (red) surface wind speed in June–July averaged from 2013–2016.  
736 Error bar indicates the standard deviation of the PCCs.



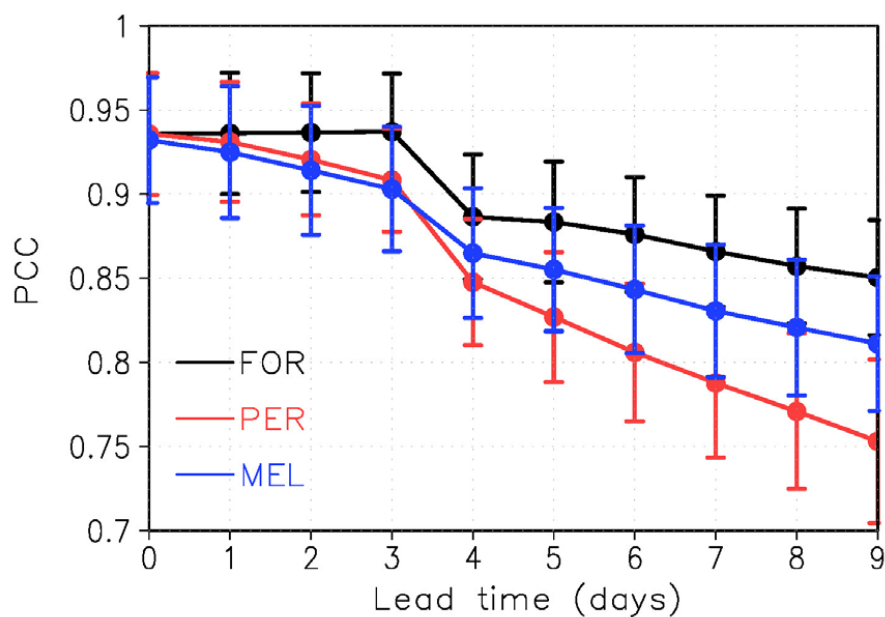
737  
 738 **Figure 8.** Temporal evolution of SIT (cm; colors) and ice velocity ( $\text{m s}^{-1}$ ; vectors) distribution for  
 739 (left) analysis, (center) forecast, and (right) the difference between forecast and analysis at increasing  
 740 lead times from +0 day to +6 days initialized on 2nd July 2015. The corresponding PCCs for the SIT  
 741 (black), zonal (red) and meridional ice speeds (blue) in the ESS (right-lower panel of the time  
 742 evolution) are shown in the lower panel. The scale for the PCCs of the zonal and meridional ice  
 743 speeds is indicated on the right axis.



744

745 **Figure 9.** (a) Relationship between 10m wind speed ( $\text{m s}^{-1}$ ) in the ERA Interim reanalysis data and  
 746 sea ice speed ( $\text{m s}^{-1}$ ) in the TOPAZ4 reanalysis averaged over a part of the ESS ( $72^{\circ}$ – $76^{\circ}$  N,  
 747  $150^{\circ}$ – $170^{\circ}$  E) during 1–31 July 2011–2014. Broken and solid lines indicate the regression line of ice  
 748 speed on 10m wind speed ( $y = 0.0224x - 0.0112$ ) and the theoretical ice speed estimated based on  
 749 classical free-drift theory, respectively. (b) Angle (degrees) of sea ice velocity relative to surface wind  
 750 vectors averaged over the ESS. Positive values indicate sea ice drift is to the right of the wind direction.  
 751 Solid curve indicates the wind–ice velocity angle estimated based on classical free-drift theory.

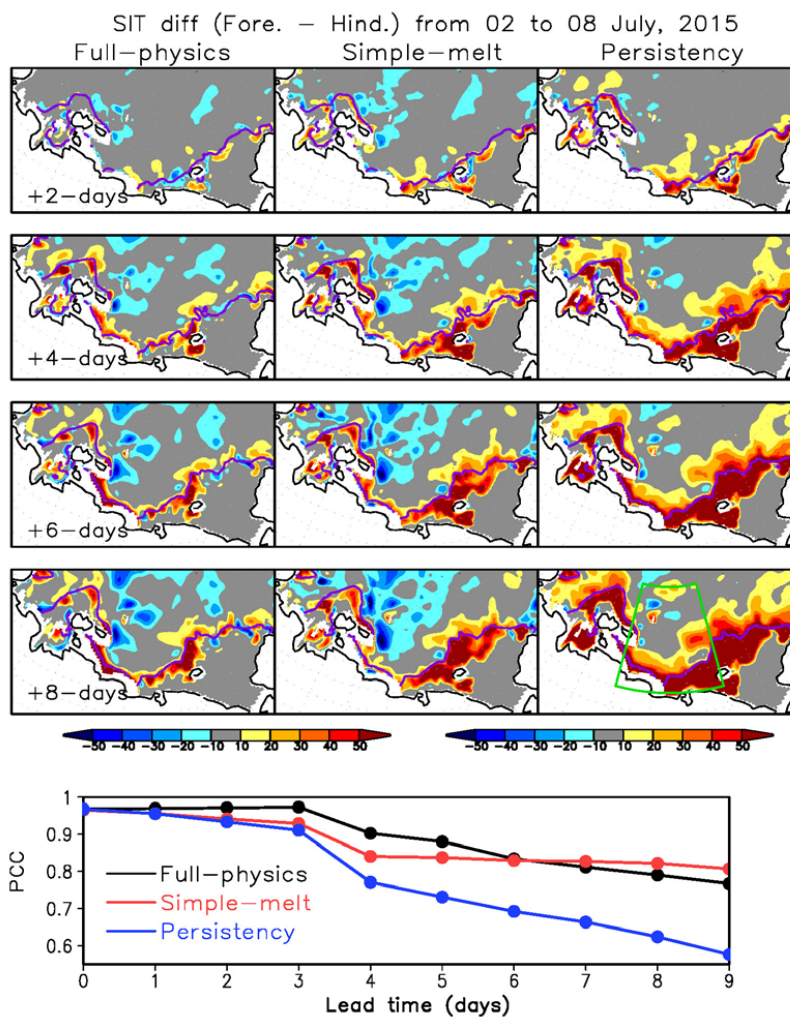
752



753

754 **Figure 10.** The PCCs between forecast and analysis SIT from the full physics model (black),  
755 persistency (red), and a simple melting model (blue) in July averaged from 2013–2016. Error bar  
756 indicates the standard deviation of the PCCs.

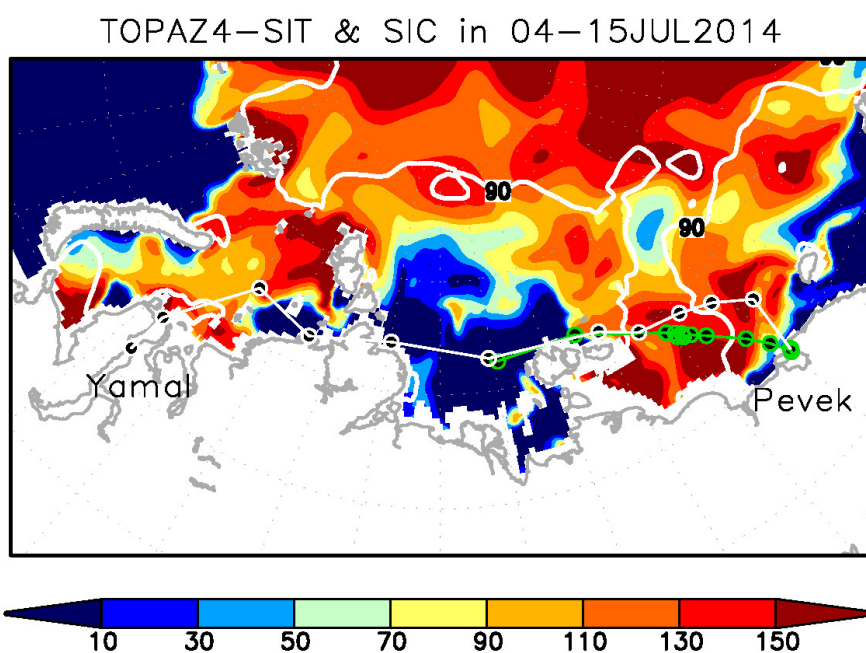
757



758

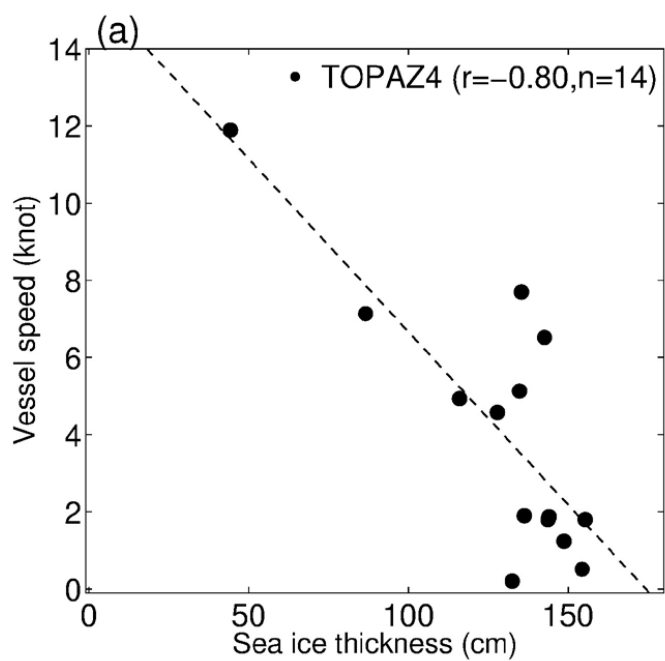
759 **Figure 11.** Temporal evolution of SIT differences (cm; colors) between the forecast and analysis data  
 760 at lead times increasing from +2 to +8 days, initialized on 2nd July 2015. In each panel, the sea ice  
 761 edge of the analysis, defined by 30% SIC, is shown. Corresponding PCCs for the full physics model  
 762 (black), a simple melting model (red) and persistency (blue) in the ESS (right-lower panel of the time  
 763 evolution) are shown in the lower panel.

764



765

766 **Figure 12.** Trajectory of the two tankers over the ESS based on AIS data. The routes cross the ESS  
767 from the Laptev Sea on 4 July 2014 to the port of Yamal on 31 July 2014, via the port of Pevek on  
768 20 July 2014. The forward route is highlighted by green circles. The SIT (cm; colors) and SIC (%;  
769 contours) averaged over the period of the forward route are shown.



770

771 **Figure 13.** Scatter plots of daily mean vessel speeds (knots) and sea ice thickness (cm) from 4–30

772 July 2014.